PHYSICAL REVIEW D
PARTICLES AND FIELDS

THIRD SERIES, VOLUME 45, NUMBER 5 1 MARCH 1992

ARTICLES

Measurement of the π^0 electromagnetic transition form factor

Reena Meijer Drees and Chris Waltham
Physics Department, University of British Columbia, Vancouver, British Columbia, Canada V6T 1Z1

Tiziano Bernasconi, Stephan Egli, Erwin Hermes, Franz Muheim, Carsten Niebuhr, Henk Pruys, and Andries van der Schaaf
Physik-Institut der Universität Zürich, CH-8001 Zürich, Switzerland

Wilhelm Bertl, Martin Grossmann-Handschin, Nicolas Lordong, Detlef Vermeulen, and H. Kristian Walter
Paul Scherrer Institut, CH-5232 Villigen PSI, Switzerland

Ralph Eichler, Larry Felawka,* Tadeusz Kozlowski,† and Stephen Playfer‡
Institut für Mittelenergiephysik der Eidgenössische Technische Hochschule Zürich, CH-5232 Villigen PSI, Switzerland

Jacques Martino
Département de Physique Nucléaire et de Hautes Energies, Centre d'Etudes Nucléaires de Saclay, 91191 Gif-sur-Yvette, France

(SINDRUM I Collaboration)

(Received 14 October 1991)

We present the result of a measurement of the π^0 electromagnetic transition form factor in the timelike region of momentum transfer. From a data sample of 54 000 $\pi^0 \to e^+e^-\gamma$ decays, observed in the SINDRUM I magnetic spectrometer at the Paul Scherrer Institute (Switzerland), we measure a value of the form factor slope $a = 0.025 \pm 0.014$ (stat) ± 0.026 (syst). This value is consistent with both the results of the recent measurement by CELLO (DESY) in the spacelike region, and with the vector-meson-dominance prediction of $a \approx 0.03$.

PACS number(s): 13.40.Hq, 13.20.Cz, 14.40.Aq

I. INTRODUCTION

The term "electromagnetic form factor" usually refers to the vertex function for the interaction of a virtual photon and a hadron. This is the simplest function that exhibits the off-mass-shell structure of hadrons, and has been studied comprehensively [1]. It is related to the charge radius of the hadron.

The charged-pion form factor is an example, and one which is well understood [2]. It has been measured in the spacelike region by electroproduction and π-e scattering experiments and in the timelike region by inverse electroproduction and e^+e^- annihilation. These data, together with the constraints of analyticity and the 1^- mass spectrum, yield a consistent picture from $q^2 = -4$ GeV^2 to $q^2 = +10$ GeV^2.

Self-conjugate pseudoscalar mesons such as the π^0 have a different class of form factor. Charge-conjugation invariance forbids the coupling of these particles to a single photon. Hence the simplest electromagnetic vertex is that shown in Fig. 1. The corresponding matrix element is given by

$$\langle \gamma(q_1,\epsilon_1), \gamma(q_2,\epsilon_2)|T|\pi^0\rangle = \frac{F}{m_\pi} f\left[\frac{q_1^2}{m_\pi^2}, \frac{q_2^2}{m_\pi^2}\right] \times \varepsilon_{\mu\nu\rho\sigma}\epsilon_1^\mu \epsilon_2^\nu q_1^\rho q_2^\sigma , \quad (1)$$

where F is a dimensionless constant and $f(q_1^2/m_\pi^2, q_2^2/m_\pi^2)$ is the π^0 form factor normalized to $f(0,0)=1$. In the approximation of a structureless particle, $f(q_1^2/m_\pi^2, q_2^2/m_\pi^2)=1$. The form factor has been studied in the "Dalitz" decay $\pi^0 \to e^+e^-\gamma$ (where $q_1^2=0$, $4m_e^2 < q_2^2 < m_\pi^2$) and in π^0 production in e^+e^- collisions (where $q_1^2 \approx 0, q_2^2 < 0$). The former method has not, until now, produced consistent results [3]. The latter method has produced one accurate result [4] consistent with theoretical expectations.

In the case of the Dalitz decay of the π^0 the form factor is determined by a measurement of the invariant-mass distribution of the e^+e^- pair, which may be calculated using quantum electrodynamics (QED), leading to the

*Present address: University of Victoria, c/o TRIUMF, Vancouver B.C., Canada V6T 2A3.

†Permanent address: Institute for Nuclear Studies, PL-05-400 Swierk, Poland.

‡Present address: Dept. of Physics, Syracuse University, Syracuse, NY.

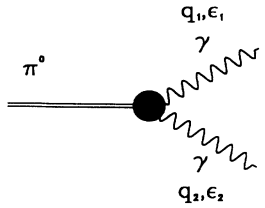

FIG. 1. The coupling of the π^0 to two photons $\gamma_{1,2}$ with momenta $q_{1,2}$ and polarizations $\epsilon_{1,2}$.

well-known Kroll-Wada formula [5,6]

$$\frac{d\Gamma}{dx}=\frac{\alpha}{3\pi}\Gamma_{\pi^0\to\gamma\gamma}\frac{(1-x)^3}{x}\left[1-\frac{r}{x}\right]^{1/2}\left[2+\frac{r}{x}\right]\times|f(0,x)|^2\,, \tag{2}$$

where $\sqrt{x}$ is the invariant mass of the e^+e^- pair, normalized to the π^0 mass, and $r=4m_e^2/m_{\pi^0}^2$. The form factor is assumed to have the form

$$f(0,x)=(1-ax)^{-1} \tag{3}$$

$$\approx 1+ax \quad \text{(for small } a\text{)}\,. \tag{4}$$

The total branching ratio of the Dalitz decay is $0.011\,98\pm0.000\,32$ [7]. Specific models are required to predict the slope parameters a of the form factor. The two common approaches are based on vector-meson dominance [8] and quark loops [9]. Both have been successful in predicting the form-factor slopes of the heavier η, η', ω, and K_L mesons [3,4,10,11,12]. In the case of the π^0 their prediction is

$$a\approx\frac{m_\pi^2}{m_\rho^2}\approx+0.03\,. \tag{5}$$

This effect will contribute to the number of events seen at maximum variant mass by an amount $2a$, i.e., 6%. The invariant-mass distribution described by (2) does not yet include the effect of "radiative corrections," higher-order Feynman diagrams involving extra internally or externally radiated photons. The change in the slope caused by these corrections is quite sensitive to the specific detector geometry and may be comparable to the predicted effect of the form factor.

A summary of the past experimental results is given in Table I. We note that since the effect of the parameter a is expected to be small, large numbers of events are necessary to obtain a statistically significant result, as well as to ensure a precise energy calibration of the detector. We choose to produce the π^0 by charge exchange ($\pi^-p\to\pi^0n$) at rest, which has a yield of approximately 60%. The resulting π^0 has a relatively low momentum of 28 MeV/c, which ensures that e^+e^- pairs of large invariant mass are emitted with large opening angles. This is advantageous for the invariant-mass resolution and for the discrimination against background from external pair production. One also expects background from the process $\pi^-p\to ne^+e^-\gamma$, at the level of a few percent.

II. EXPERIMENTAL SETUP AND ON-LINE EVENT SELECTION

The πE3 channel at the Paul Scherrer Institute (Switzerland) provided a beam of 95-MeV/c negative pions, which were stopped in liquid hydrogen to produce the π^0's. The target cell was a 12-cm-long, 19-mm-radius Mylar cylinder (0.12 mm wall thickness), concentric with the beam axis and capped with a hemisphere at the upstream end. The Makrolon vacuum window surrounding the hydrogen target had a radius of 25 mm and a thickness of 0.7 mm. The center of the hemisphere capping the target was located 10 cm upstream of the center of the SINDRUM I magnetic spectrometer to optimize the acceptance for an associated measurement of the $\pi^0\to e^+e^-$ branching ratio [20]. The π^- beam passed through a 5-mm-thick lead moderator giving the highest stop density at the beginning of the target. About 10% of the incident π^- stopped in the first 5 cm of the target. The stop rate was limited to 10^4 s^{-1} to match the capacity of the data-acquisition system.

The SINDRUM I spectrometer was equipped with five cylindrical proportional chambers and a scintillating hodoscope as shown in Fig. 2. Three of the wire chambers provided z information. A description can be found in Ref. [20]. The magnetic field was 0.33 T, resulting in a transverse-momentum threshold of roughly 17 MeV/c for particles to reach the scintillator hodoscope.

TABLE I. Previous measurements. Summary of previous experiments to measure the π^0 transition form factor. The results of Samios, Kobrak, and Devons do not include radiative corrections. The CELLO measurement is in the region of spacelike momentum transfer; the others are for timelike momentum transfer. Errors are combined statistical and systematic, except where indicated separately. The Fischer group quote a *statistical error only.*

Reference	No. of events	a
Samios *et al.*, 1961 [13]	3071	$a=-0.24\pm0.16$
Kobrak *et al.*, 1961 [14]	7676	$a=-0.15\pm0.10$
Devons *et al.*, 1969 [15]	2200	$a=+0.01\pm0.11$
Burger *et al.*, 1975 [16]	2437	$a=+0.02\pm0.10$
Fischer *et al.*, 1978 [17]	31 458	$a=+0.10\pm0.03$
Fonvieille *et al.*, 1989 [18]	36 699	$a=-0.11\pm0.03\pm0.08$
Farzanpay *et al.*, 1991 [19]	10 009	$a=+0.026\pm0.024\pm0.048$
CELLO Collaboration, 1991 [4]	137	$a=0.0326\pm0.0026$

The inner chamber defined a lower threshold for the detection of hits from additional charged particles of between 1 and 3 MeV/c, depending on vertex position and emission angle.

A programmable FASTBUS track preselector was used to search for track candidates in the pattern of the hodoscope strips and groups of 8 or 16 anode wires. For each track the angle of emission was stored. From this information the transverse opening angle ϕ was calculated by a general purpose FASTBUS processor with a mean decision time of 50 μs. The opening angle is defined such that if ϕ is more than 180° the two tracks bend towards each other and if ϕ is less than 180° they move apart (see Fig. 2). The trigger for data readout required an e^+e^- pair with $35° < \phi < 260°$. The upper cut removes events in which the two tracks might cross each other in the r-φ plane, which could cause errors in the reconstruction. The lower cut removes a large fraction of events at low invariant mass with a minimal increase in statistical error for the slope a.

Before going to tape, the data were filtered by a full analysis of the information in the r-φ projection. The filter program required an e^+e^- pair with a hodoscope time difference within 1.6 ns and an r-φ opening angle within the same limits as those imposed nominally by the trigger. Of all $\pi^0 \to e^+e^-\gamma$ decays, 1.5% satisfied the trigger requirements. The final event rate was about 1 Hz, of which roughly 50% was due to Dalitz decays, 25% was due to the $\pi^- p \to n e^+ e^-$ background, and the rest was from photon conversions in the moderator, target support structure, and inner chamber.

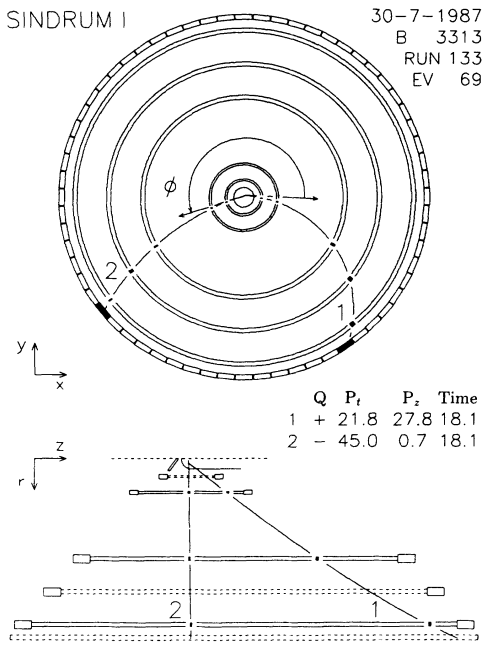

FIG. 2. A candidate $\pi^0 \to e^+e^-\gamma$ event in the x-y and z-r projections. The target cell, the five proportional chambers, and the 64-fold scintillator hodoscope are depicted. The outer radius of the hodoscope is 35 cm. The convention for the transverse opening angle is indicated. The results of the event-reconstruction program for the particle trajectories and the corresponding track parameters charge, momentum (MeV/c), and hodoscope time (ns) are shown.

Three significant data runs were performed (labeled "runs 1, 2, and 3"), between which the detector was partially dismantled for repairs to the wire chambers. After track reconstruction the three runs comprise 23 559, 107 862, and 23 222 events (consisting of $\pi^0 \to e^+e^-\gamma$, $\pi^- p \to n e^+ e^-$, and conversion events), respectively. The total data-taking time was approximately three days.

III. MONTE CARLO SIMULATION

Successful determination of the slope parameter a requires the accurate description of the various reactions. Events were generated with the proper phase-space distributions and the response of the spectrometer was simulated [21] using the GEANT package [22] available from CERN. We highlight the points crucial to an accurate form-factor measurement: (1) accurate modeling of the π^- stopping distribution in the target; (2) precise description of the geometry of the detector; (3) accurate calculation of the $\pi^0 \to e^+e^-\gamma$ matrix element, including higher-order radiative corrections; (4) careful assessment of background processes.

Since the acceptance of the spectrometer depends on the vertex position, the π^- stopping distribution must be reproduced for each run. The acceptance is independent of φ, so it is sufficient to reproduce the distribution in r-z. Using an iterative approach we match the measured vertex distribution shown in Fig. 3.

We choose the $\pi^0 \to e^+e^-\gamma$ decay events according to the Kroll-Wada matrix elements [6], with the form-factor slope a set to zero. We must also include the higher-order radiative corrections, as discussed previously. We use the code developed by Roberts and Smith [23] (checked against the semianalytical results of Mikaelian and Smith [24]) which calculates the matrix elements for both $\pi^0 \to e^+e^-\gamma\gamma$ and the internal radiative processes.

Table II lists the sources of background which we simulate, together with their resultant contamination of the $\pi^0 \to e^+e^-\gamma$ sample. To model the $\pi^0 \to e^+e^-e^+e^-$ background, we use the matrix element calculated by Miyazaki and Takasugi [25]. The contributions from the external conversion processes are calculated by forcing

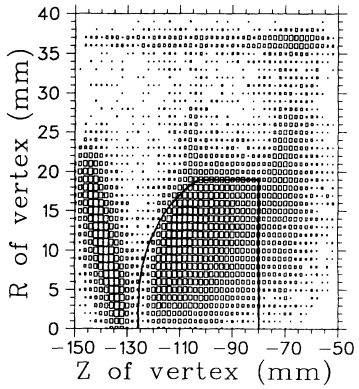

FIG. 3. The vertex distribution in r and z for all pairs of tracks with opposite curvature. The solid line indicates the vertex cut applied in the off-line analysis.

TABLE II. Backgrounds. Background processes considered and their calculated contribution to the total sample, which numbers roughly 54 000 events. Conversions are modeled in the liquid hydrogen target, in the target walls, and in chamber 1.

Process	Contribution to class A events
$\pi^0 \to e^+e^-e^+e^-$	<5
$\pi^0 \to e^+e^-\gamma$ (Compton)	<10
$\pi^0 \to e^+e^-\gamma$ (pair prod.)	<5
$\pi^0 \to \gamma\gamma$ (pair prod.)	<3
$\pi^0 \to \gamma\gamma$ (2×pair prod.)	<5
$\pi^0 \to \gamma\gamma$ (Compton+pair prod.)	<10
$\pi^- p \to n\gamma$ (pair prod.)	<3
$\pi^- p \to n e^+ e^- \gamma$	1200±250

the photon to undergo either pair production or Compton scattering, and subsequently weighting the event by the probability of its occurrence. We find no significant contamination from any external photon conversion processes, nor from the double Dalitz decay $\pi^0 \to e^+e^-e^+e^-$. We ignore these backgrounds in what follows.

The largest source of background is due to the process $\pi^- p \to n e^+ e^- \gamma$, in which the radiated photon carries away enough energy to move the event into the kinematical region occupied by the Dalitz decay (see Fig. 4). It is therefore imperative that this reaction be simulated and added to the $\pi^0 \to e^+e^-\gamma$ Monte Carlo sample.

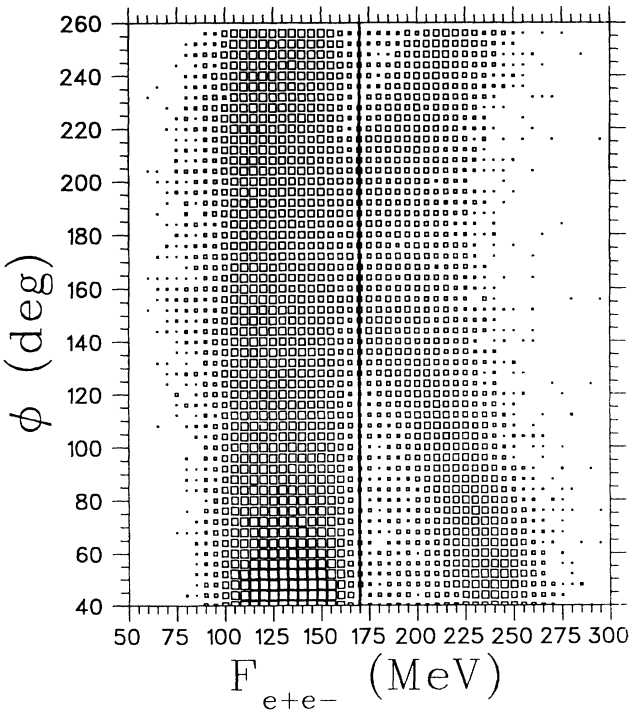

FIG. 4. Distribution of $F_{e^+e^-}$ versus opening angle ϕ of the e^+e^- pair for the measured data. The boxlike distribution of the Dalitz events is clearly visible. The slanted bands are populated by the $\pi^- p \to n e^+ e^-$ events. The cut separating class A data from class B data is shown.

No exact theoretical calculations of the $\pi^- p \to n e^+ e^- \gamma$ reaction have been done; however, approximate methods, such as those used by Fonvieille *et al.*, which are accurate to approximately 20% [18], may be used.

The simulated data was passed through a trigger and filter simulation program, and was subsequently analyzed in an identical manner to the real data.

IV. OFF-LINE ANALYSIS

The reconstruction of the recorded events was done in three steps. First track candidates were searched in the r-φ projection. Only tracks with hits in all five chambers and the scintillator hodoscope were accepted. In a second step the z information from the three chambers with cathode strips was used to determine the polar emission angle θ. Tracks with less than two z values were rejected. In a third step electron-positron pairs were selected with a hodoscope time difference below 1 ns and a distance of closest approach to a vertex below 1.3 mm. The total reconstruction efficiency for the events of interest was 96±1%.

In order to obtain a clean sample of e^+e^- pairs originating in the target and from a well-defined region of phase space the following cuts were made.

(1) *Cuts on the vertex position.* The distribution of the vertex position in r and z is shown in Fig. 3. The contour indicates the region allowed in the event selection. This cut removed external conversion events from the lead degrader positioned just in front of the target, and those from the vacuum cylinder and inner chamber, altogether about 25% of the sample.

(2) *Cuts superseding the action of the trigger and threshold.* Not all tracks leaving the target and reaching the hodoscope were accepted by the trigger. Losses occurred mainly at the extremes of the transverse-momentum distribution. In addition the resolution in angle was limited. In order to minimize uncertainties introduced by the trigger the acceptance was further reduced by the requirements $p_t > 20$ MeV/c and $45° < \phi < 260°$ for runs 2 and 3, and $45° < \phi < 220°$ for run 1 (an early run to establish the trigger conditions).

(3) *Cut on muon events.* $\mu \to e\nu\bar{\nu}$ decays in which the electron passes from one side of the hodoscope to the other (mimicking an e^+e^- pair with a 180° opening angle) are removed by the requirement that the two hodoscope hits be simultaneous. In order to eliminate the last few remaining events we require the reconstructed total pair momentum $|\mathbf{p}_{e^+e^-}| > 10$ MeV/c. This cut removes 0.5% of the Dalitz events.

(4) *Chamber multiplicity cuts.* The requirement that the inner two chambers of SINDRUM exhibit two and only two hits greatly suppresses contamination by external conversion processes, in which photons from $\pi^0 \to \gamma\gamma$ or $\pi^0 \to e^+e^-\gamma$ undergo pair production or Compton scattering in the degrader, target, target wall, vacuum cylinder or innermost chamber. This cut also removes background from the $\pi^0 \to e^+e^-e^+e^-$ decay.

(5) *Fiducial chamber cuts.* The magnetic field was uniform to better than 1% within the central section of the

chambers [26]. By excluding tracks which pass through the outer 12 cm on the upstream and downstream ends of the middle chamber, we define a fiducial volume inside this region.

Momentum calibration. We have calibrated the effective mean value of the magnetic field using both the sample of $\pi^0 \to e^+e^-\gamma$ events and the $\pi^- p \to n e^+ e^-$ events. For this purpose the following two quantities were defined:

$$T_{\rm tot} = T_{e^+} + T_{e^-} + T_n$$

and

$$F_{e^+e^-} = E_{e^+e^-} + |\mathbf{p}_{e^+e^-}| c \ , \tag{6}$$

where the kinetic energy of the neutron T_n has been calculated under the assumption that the missing momentum is carried by the neutron only. Neglecting radiative corrections, for $\pi^- p \to n e^+ e^-$ events $T_{\rm tot} = \sqrt{s} - m_n c^2 - 2 m_e c^2 \approx 138$ MeV. For Dalitz decays the quantity $F_{e^+e^-}$ reaches a minimum of $(1-\beta_{\pi^0}) E_{\pi^0} = 110$ MeV when the photon and neutron move in opposite directions, and a maximum of $(1+\beta_{\pi^0}) E_{\pi^0} = 166$ MeV when they move in the same direction. Since radiative corrections may lead to the emission of an additional energetic photon, low-energy tails occur. Figure 4 shows the distribution of $F_{e^+e^-}$ versus transverse opening angle (an independent quantity), and clearly shows the boxlike distribution of the Dalitz decays, including the low-energy radiative tail. Also visible are the slanted bands containing the $\pi^- p \to n e^+ e^-$ events. A cut at $F_{e^+e^-} = 170$ MeV, as illustrated in Fig. 4, divides the events into two samples: "class A" events containing mainly $\pi^0 \to e^+e^-\gamma$ events with a small contamination from $\pi^- p \to n e^+ e^- \gamma$ and "class B" events, comprising mainly $\pi^- p \to n e^+ e^-$ events.

The value of the magnetic field was determined from the distributions of $F_{e^+e^-}$ and $T_{\rm tot}$ for class A and B events, respectively, as shown in Figs. 5 and 6 for run 2. Note the good agreement between simulated and measured distributions, especially in the regions of the low-energy tails, which demonstrates the proper treatment of the radiative corrections. For class A data, it is necessary to include the contaminant $\pi^- p \to n e^+ e^- \gamma$ events. The relative contribution (λ) of the simulated $\pi^- p \to n e^+ e^-$ events has been treated as a free parameter, determined by fitting the missing energy distribution of the entire data sample (class A plus class B), as shown in Fig. 7. The fitted magnetic field, normalized to its nominal value, is shown in Table III for each run and for both event classes separately. The mean deviation from 1 is about 0.2%, consistent with the absolute accuracy of the power supply. The results from the two event classes are consistent.

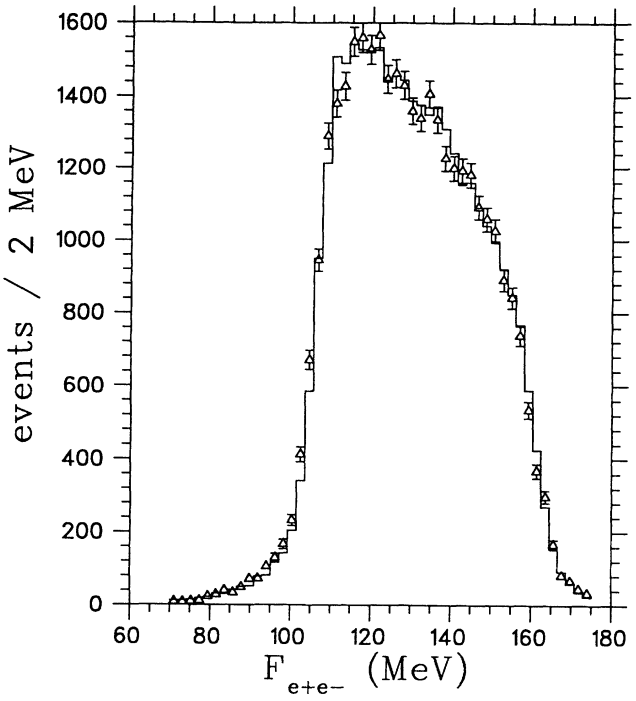

FIG. 5. The distributions of $F_{e^+e^-}$ for class A events of measured (triangles) and simulated (line) data. In the simulated distribution we include higher-order radiative processes as well as contamination from $\pi^- p \to n e^+ e^- \gamma$.

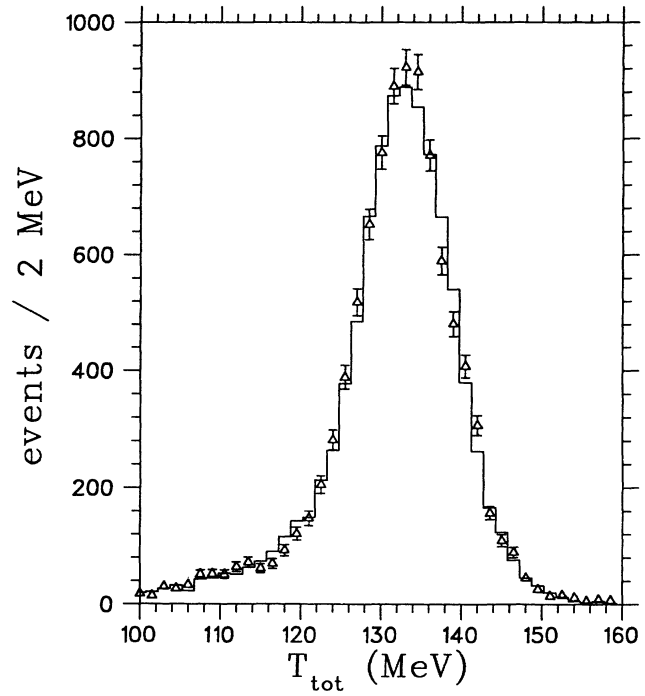

FIG. 6. The distributions of $T_{\rm tot}$ for class B events of measured (triangles) and simulated (line) data. Radiative processes have been taken into account. The low-energy tail is understood to roughly 20%.

V. EXTRACTION OF THE SLOPE PARAMETER *a*

We fit for the slope parameter a using class A data, which consists of $\pi^0 \to e^+e^-\gamma$ and $\pi^0 \to e^+e^-\gamma\gamma$ events

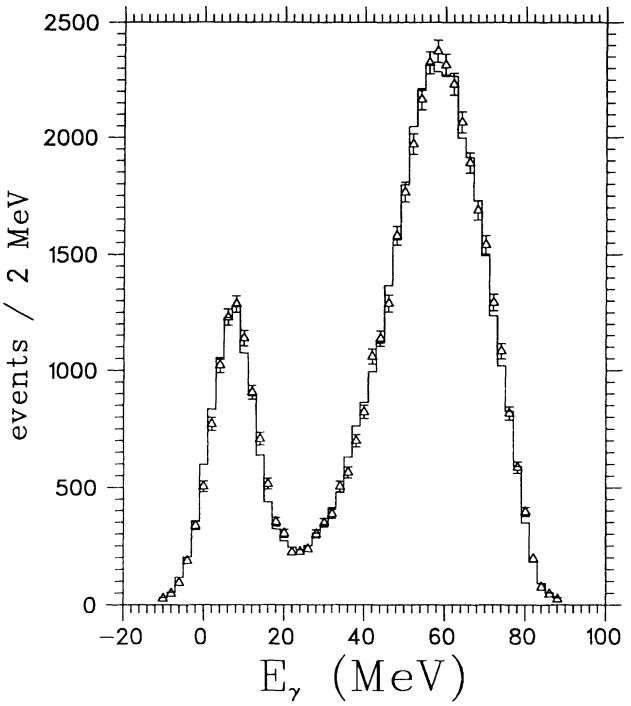

FIG. 7. The distribution of the missing energy E_γ for measured (triangles) and simulated (line) data for the total sample. In the simulated distribution the contribution of $\pi^- p \to n e^+ e^-$ relative to $\pi^0 \to e^+ e^- \gamma$ has been treated as a free parameter (λ).

plus the $\pi^- p \to n e^+ e^- \gamma$ events. Our understanding of the $\pi^- p \to n e^+ e^-$ and $\pi^- p \to n e^+ e^- \gamma$ events is demonstrated in Figs. 6 and 8. Figure 6 shows the total kinetic energy of the $e^+ e^-$ pair in $\pi^- p \to n e^+ e^-$ and $\pi^- p \to n e^+ e^- \gamma$; the radiative tail is clearly visible, and is generally well fit by the Monte Carlo simulation. The overall performance of the $\pi^- p \to n e^+ e^-$ and $\pi^- p \to n e^+ e^- \gamma$ (class B) simulation for run 2 may be seen in Figs. 8(a) through 8(g). In Figs. 9(a) through 9(g) we show the performance of the simulation of class A events for various parameters. The agreement is good, and we may proceed to extract a.

The value of a has been fitted to the distribution of the reconstructed value of x for class A events. The measured distribution $N_{\rm meas}(x_i)$ is compared to a predicted distribution $N_{\rm pred}(x_i)$, defined as

$$N_{\rm pred}(a,x_i) \equiv \kappa [N_{e^+e^-\gamma}(a,x_i) + \lambda N_{ne^+e^-\gamma}(x_i)] , \quad (7)$$

where the index i represents the bin number. Since the normalization constant κ is treated as a free parameter,

TABLE III. Magnetic field calibration. Results of the magnetic field calibrations for the various runs. We indicate the fitted field value, normalized to its nominal magnitude. The magnet was turned off and on between the various runs.

Run	$e^+e^-\gamma$ calibration	ne^+e^- calibration
1	1.0020±0.0010	1.0012±0.0010
2	1.0024±0.0005	1.0028±0.0005
3	1.0032±0.0010	1.0012±0.0010

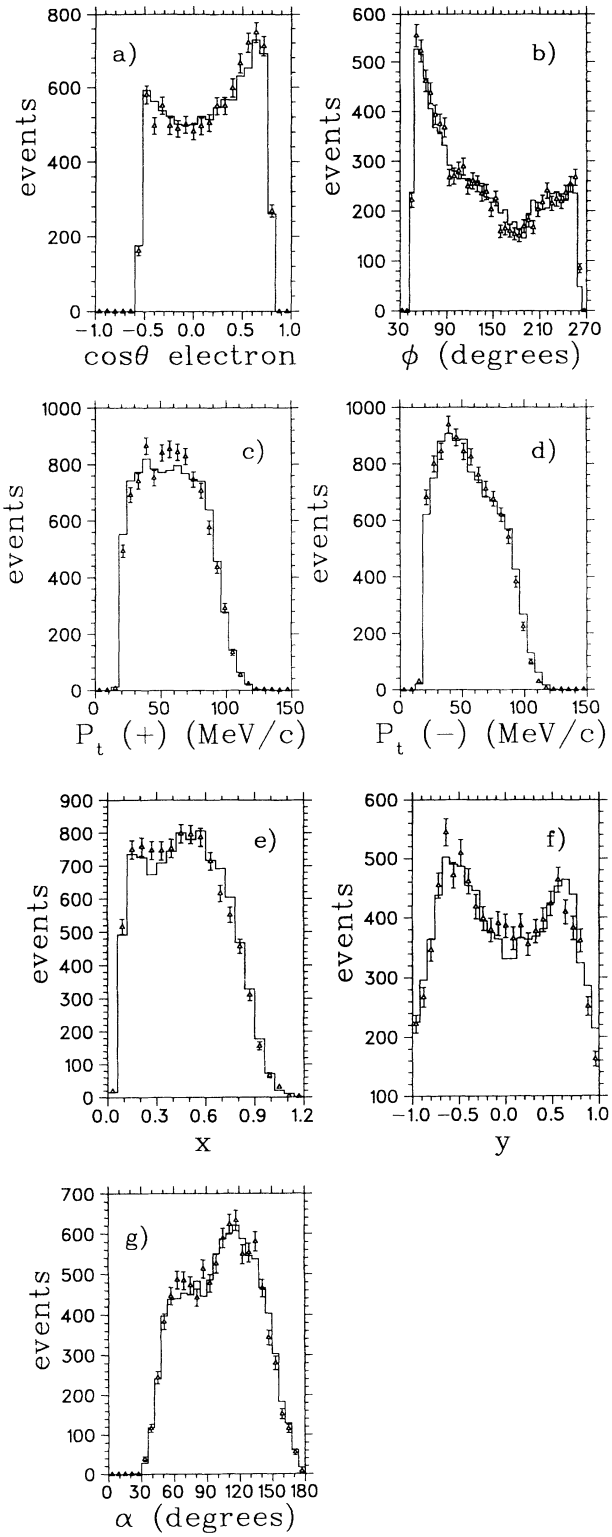

FIG. 8. Comparison of various measured (triangles) and simulated (line) distributions of class B events from run 2: (a) $\cos\theta$ of the electron, (b) transverse opening angle ϕ, (c) transverse momentum of the positron, (d) transverse momentum of the electron, (e) invariant mass of the pair, (f) energy partition $y = (E_- - E_+)/|\mathbf{p}_{e^+e^-}|$ and (g) opening angle α. The difference in momentum distribution for the two charges is due to the trigger.

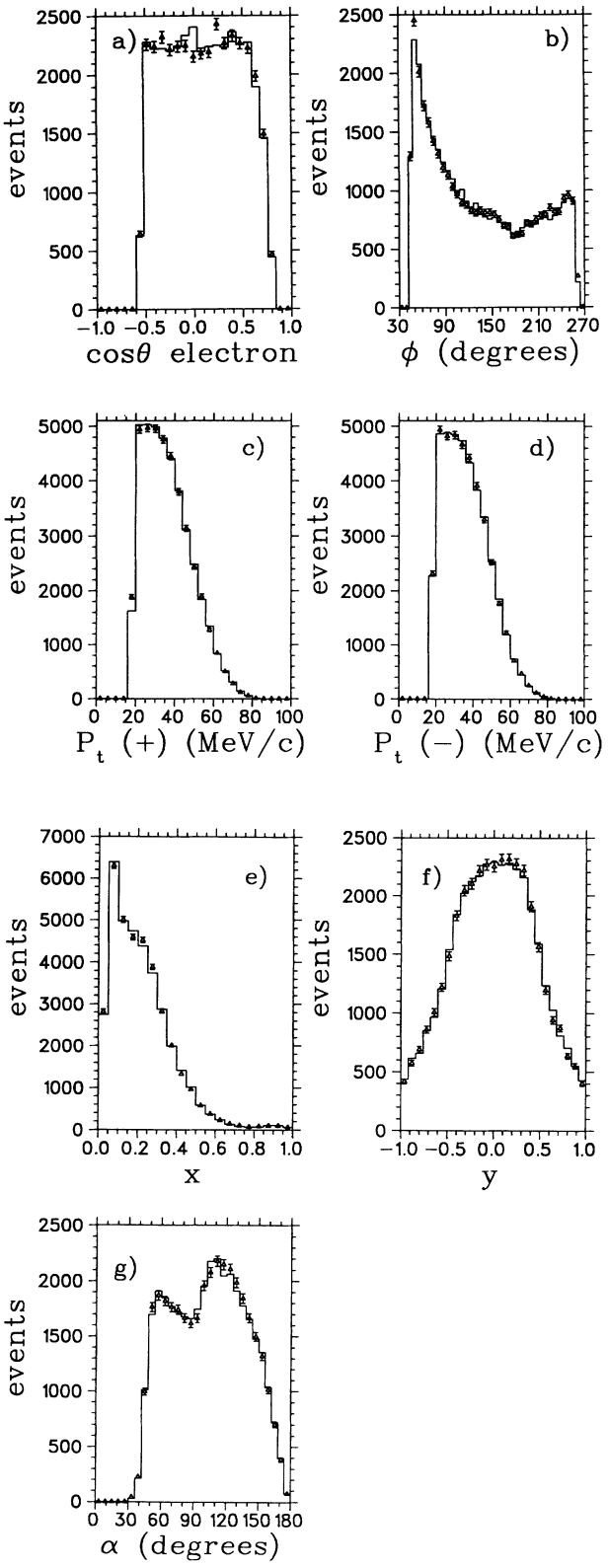

FIG. 9. Comparison of various measured (triangles) and simulated (line) distributions of class A events from run 2: (a) $\cos\theta$ of the electron, (b) transverse opening angle ϕ, (c) transverse momentum of the positron, (d) transverse momentum of the electron, (e) invariant mass of the pair, (f) energy partition $y=(E_- - E_+)/|\mathbf{p}_{e^+e^-}|$ and (g) opening angle α.

the analysis does not depend on the knowledge of the number of pions stopped in the target. The relative contribution λ from the reaction $\pi^- p \to n e^+ e^- \gamma$ has been determined independently, as discussed in the previous section. The predicted distribution of Dalitz events has been approximated by

$$N_{e^+e^-\gamma}(a,x_i) \approx N_{e^+e^-\gamma}(0,x_i) + 2a\hat{N}_{e^+e^-\gamma}(0,x_i) \ . \quad (8)$$

In the distribution $\hat{N}_{e^+e^-\gamma}(0,x_i)$ every event is weighted by the value for x which has been used as input in the event generation.

The most likely values for a and κ have been determined by χ^2 minimization. The minimum χ^2 per degree of freedom is typically 1.3. Figure 10 shows the fractional difference between the real and simulated data as a function of x. There is no clear evidence for any nonlinear form-factor effects.

VI. EVALUATION OF SYSTEMATIC ERRORS

Systematic errors arise from inaccurate knowledge of the behavior of the detector or imperfect knowledge of the theoretical distributions for the processes of interest. Possible contributions may be classed into run-dependent and run-independent errors.

A. Run-dependent systematic errors

By varying run-dependent quantities and reanalyzing the data, the systematic error due to each may be determined. The results are given in Table IV. A brief description of each contribution follows.

(1) *Magnetic field.* There is a systematic error in a due to our imperfect knowledge of the value of the magnetic

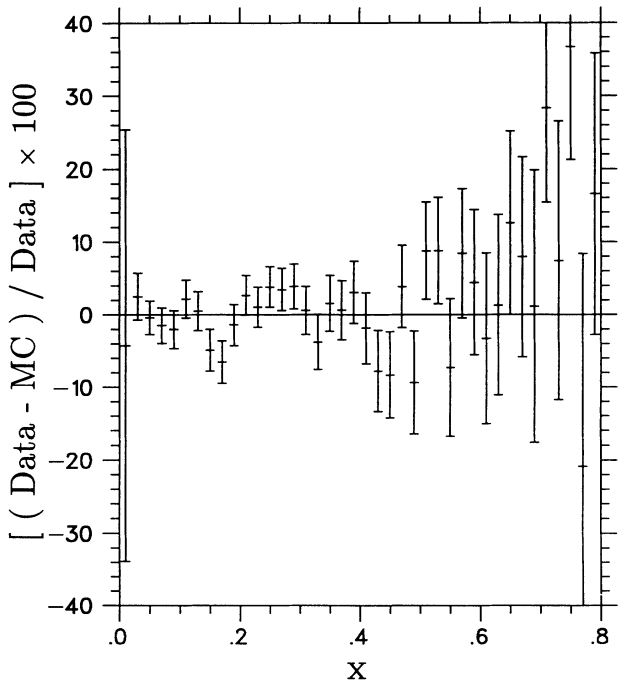

FIG. 10. The dependence of $R(x) \equiv N_{\text{meas}}(x)/N_{\text{pred}}(x) - 1$ on x. $N_{\text{pred}}(x)$ was calculated assuming $a=0.025$. There is no clear evidence for nonlinear form-factor effects.

TABLE IV. Systematic errors. Systematic errors from various sources. The table is divided into run-dependent errors (top) and run-independent errors (bottom).

Error source	Error contribution
Magnetic field	0.010
Stop distribution	0.005
Target location	0.005
Chamber Δx, Δy, Δz, $\Delta\phi$	0.020
Run-dependent total	0.023
Chamber construction	$\ll 0.003$
Hardware trigger	0.005
Analysis cuts	0.010
$ne^+e^-\gamma$	0.001
$e^+e^-\gamma$ radiative corrections	0.0015
Run-independent total	0.011
Overall total	0.026

field, which is on the order of 0.2%. An error in the field of this magnitude would change a by 0.010.

(2) *Stop distribution.* We adjust the transverse scale of the stop distribution until the data and simulation are on the margin of compatibility (within statistics) and fit for a. Such a change in mean transverse vertex position, $\Delta\bar{r}_v = 0.06$ mm, gives $\Delta a = 0.005$.

(3) *Target location.* We calibrate the position of the target along the detector axis (z) by examining the external conversion events in the raw data. The lead degrader is clearly visible, as is the target's aluminum support ring. These items are fixed to the target, whose position can thereby be determined to approximately 2 mm. Moving the target by this amount in the simulation gives $\Delta a = 0.005$.

(4) *Chamber locations.* The chambers can be offset in x, y, z, and φ. In this case we are concerned with the position of chambers 1–4 relative to chamber 5, as an offset of all chambers is clearly equivalent to a shift in target position. The offsets may vary from run to run as the chambers were remounted each time; they are determined by analysis of cosmic-ray data with no magnetic field. The chamber positions have been calibrated to 0.5 mm, and the rotations to 0.1°. We vary the calibrations accordingly and redo the track fitting. The position of middle chamber 3 is the most crucial single variable as it fixes the curvature of the track, and the offset in φ has the most effect on the measured momenta; for a $\Delta\varphi = 0.1°$, $\Delta a = 0.010$. The total error from such sources is conservatively estimated to be 0.020.

B. Run-independent systematic errors

The run-independent systematic errors must also be evaluated, and will increase the overall error on the final results as shown in Table V. We elaborate briefly on the evaluation of these.

(1) *Chamber construction.* The chambers exhibit twists and wire spacing irregularities, which are constant from run to run. Twists occur when one end of the chamber is rotated slightly about its axis relative to the other end.

TABLE V. Results. Summary of the fit results for each run. Single errors are statistical. The summary value given is the error-weighted average, and the errors quoted are the statistical and estimated systematic values, respectively.

Run	a	No. of events
1	0.026±0.036	7895
2	0.007±0.017	38278
3	0.076±0.029	7782
All	0.025±0.014±0.026	53955

These are small in comparison to the aforementioned offsets, and hence they are not modeled explicitly but are included in the track reconstruction of the measured data only. The effect of the twists on a with no corrections is only 0.003, so when the corrections are applied, the contribution to the total error is expected to be negligible.

(2) *Hardware trigger.* The hardware trigger applies a window in transverse opening angle and a charge asymmetric momentum window. The upper threshold on the momentum is not very precisely defined and reduces the rate of ne^+e^- events by a larger amount than the Dalitz sample. The action of the trigger with respect to the relative acceptance for class A and B data sets can be compared to theoretical branching ratios and it is understood to within 2%. If it is changed by this amount, a changes by 0.005.

(3) *Analysis cuts.* The analysis cuts are constant from run to run. We find that the variation of a with changes in cuts in vertex position, ϕ and $|\mathbf{p}_{e^+e^-}|$, is small if these changes are the same size as the accuracy with which these quantities are known. If the radial vertex cuts are moved in or out by 0.25 mm (in the data only), $\Delta a = 0.003$; if the ϕ cut is changed by 0.1°, $\Delta a \ll 0.001$; if the $|\mathbf{p}_{e^+e^-}|$ cut is changed by 100 keV/c, $\Delta a = 0.001$. If these cuts are changed in both data and simulation, the value of a is stable for changes a factor of 20 larger than those quoted above.

Systematic errors are possible due to the multiplicity cuts on the inner chambers. However, the hit multiplicity distributions are well reproduced by the Monte Carlo calculations over the range of energies and emission angles encountered. This has been checked with the $\pi^-p \to ne^+e^-$ sample; the multiplicity cuts make a small difference to the shape of the distributions in x and opening angle α. If this were expressed as a slope factor in an identical manner to that of the Dalitz decay, the change caused by the multiplicity cut would be $\Delta a = 0.01$. This is a dominant error introduced by the analysis procedure.

(4) *Contamination from* ne^+e^-. The $\pi^-p \to ne^+e^-\gamma$ events contaminate the Dalitz sample. We can calculate the size of this radiative tail to within 20%, and fit it where it is visible to an accuracy of 2%. By changing the number of ne^+e^- tail events by 2% and reanalyzing the data, we obtain $\Delta a = 0.001$.

(5) *Radiative corrections to* $\pi^0 \to e^+e^-\gamma$. The results of the numerical integration of the matrix elements of the $\pi^0 \to e^+e^-\gamma$ radiative corrections have been checked against published semianalytical values [24], and agree to within 5%. Furthermore, the radiative tail in $F_{e^+e^-}$ is

very well modeled. The total effect of the radiative corrections is $\Delta a = 0.03$, so the systematic error induced by the uncertainty in the $\pi^0 \to e^+e^-\gamma$ radiative corrections is small, ≈ 0.0015. These results have been checked using the e^+e^- opening angle (α) distribution, which has a smaller dependence of a but where the effects of radiative corrections are much larger. The results for a from both x and α distributions agree within statistics *only* when radiative corrections are applied. Without the corrections they disagree by three standard deviations. This gives us confidence that higher-order processes are treated correctly.

C. Other systematic checks

In addition to estimating the values for the systematic errors listed in Table IV we studied the influence of the geometric acceptance of SINDRUM by selecting events from different angular regions. These subsets give results for a which are consistent within their statistical and run-dependent systematic errors.

We also determine a using the e^+e^- opening angle (α) distribution, as noted above. Although the systematic errors are distributed differently from those in the x analysis, the two results for a are consistent.

The variation in a from run to run (rms deviation is 0.031, see Table V) is consistent with our estimated statistical and run-dependent systematic errors.

In conclusion, the largest contribution to the systematic error comes from our incomplete knowledge of the relative chamber positions. The knowledge of the magnetic field and the uncertainty in the chamber multiplicity cuts are also significant.

VII. RESULTS AND CONCLUSIONS

From the final fit results listed in Table V, we obtain a combined result:

$$a = 0.025 \pm 0.014(\text{stat}) \pm 0.026(\text{syst}) \quad (4m_e^2 < q^2 < m_\pi^2) . \quad (9)$$

This result improves on previous timelike measurements of the π^0 decay and is in accord with both the vector-meson prediction of $a = 0.03$ and the spacelike measurement from CELLO of $a = 0.0326 \pm 0.0026 (-2.5\ \text{GeV}^2 < q^2 < -0.5\ \text{GeV}^2)$.

ACKNOWLEDGMENTS

We thank Helène Fonvieille and Lee Roberts for their extremely helpful comments concerning the radiative corrections. This work was supported by the Swiss National Science Foundation and by the Natural Science and Engineering Research Council of Canada (NSERC). One of us (R.M.D.) is grateful to the NSERC for financial support.

[1] M. Gourdin, Phys. Rep. **11**, 29 (1974).
[2] M. F. Heyn and C. B. Lang, Z. Phys. C **7**, 169 (1981).
[3] L. G. Landsberg, Phys. Rep. **128**, 301 (1985).
[4] CELLO Collaboration, H.-J. Behrend *et al.*, Z. Phys. C **49**, 401 (1991).
[5] R. H. Dalitz, Proc. Phys. Soc. **A64**, 667 (1951).
[6] N. M. Kroll and W. Wada, Phys. Rev. **98**, 1355 (1955).
[7] Particle Data Group, J. J. Hernández *et al.*, Phys. Lett. B **239**, 1 (1990).
[8] G. Barton and B. G. Smith, Nuovo Cimento **36**, 436 (1965).
[9] Ll. Ametller, L. Bergström, A. Bramon, and E. Massó, Nucl. Phys. **B228**, 301 (1983).
[10] M. R. Jane, P. Grannis, B. D. James, N. H. Lipman, D. P. Owen, V. Z. Peterson, W. T. Tone, E. H. Bellamy, M. G. Green, C. Solomonides, J. A. Strong, and D. H. Thomas, Phys. Lett. **59A**, 103 (1975).
[11] Yu. B. Bushnin *et al.*, Phys. Lett. **79B**, 147 (1978); R. I. Dzhelyadin *et al.*, *ibid.* **88B**, 379 (1979); **84B**, 143 (1979); **94B**, 548 (1980); **102B**, 296 (1981).
[12] NA31 Collaboration, G. D. Barr *et al.*, Phys. Lett. B **240**, 283 (1990).
[13] N. P. Samios, Phys. Rev. **121**, 275 (1961).
[14] H. Kobrak, Nuovo Cimento **20**, 1115 (1961).
[15] S. Devons, P. Némethy, C. Nissim-Sabat, E. DiCapua, and A. Lanzara, Phys. Rev. **184**, 1356 (1969).
[16] J. Burger, Doctoral thesis, Columbia University, New York, Physics, 1972.
[17] J. Fischer, J. P. Extermann, O. Guisan, R. Mermod, L. Rosselet, R. Sachot, P. Bloch, G. Bunce, B. Devaux, A. M. Diamant-Berger, N. Do-Duc, G. Marel, and R. Turlay, Phys. Lett. **79B**, 359 (1978).
[18] H. Fonvieille, Doctoral thesis, L'Université Blaise Pascal-Clermont II, Clermont-Ferrand, France, 1989; Phys. Lett. B **233**, 65 (1989).
[19] F. Farzanpay, P. Gumplinger, A. Stetz, I. Blevis, J.-M. Poutissou, M. Hasinoff, C. J. Virtue, C. E. Waltham, B. C. Robertson, T. Mulera, A. Shor, S. H. Chew, and J. Lowe (unpublished).
[20] SINDRUM Collaboration, C. Niebuhr, R. Eichler, L. Felawka, T. Kozlowski, S. Playfer, H. K. Walter, A. van der Schaaf, S. Egli, M. Grossmann-Handschin, E. Hermes, F. Muheim, H. Pruys, D. Vermeulen, W. Bertl, N. Lordong, J. Martino, R. Meijer Drees, C. E. Waltham, and U. Bellgardt, Phys. Rev. D **40**, 2796 (1989).
[21] R. Meijer Drees, Ph.D thesis, University of British Columbia, 1991.
[22] GEANT3 User's Guide, CERN Data Handling Division, DD/EE/84-1 (1986).
[23] L. Roberts and J. Smith, Phys. Rev. D **33**, 3457 (1986).
[24] K. O. Mikaelian and J. Smith, Phys. Rev. D **5**, 1763 (1972); **5**, 2890 (1972).
[25] T. Miyazaki and E. Takasugi, Phys. Rev. D **8**, 2051 (1973).
[26] SINDRUM Collaboration, W. Bertl, S. Egli, R. Eichler, R. Engfer, L. Felawka, Ch. Grab, E. A. Hermes, N. Kraus, N. Lordong, J. Martino, H. Pruys, A. van der Schaaf, and H. K. Walter, Nucl. Phys. **B260**, 1 (1985).